

The effect of recombination radiation on the temperature and ionization state of partially ionized gas

Milan Raičević^{1*}, Andreas H. Pawlik², Joop Schaye¹, Alireza Rahmati¹

¹*Leiden Observatory, Leiden University, P.O. Box 9513, 2300 RA Leiden, The Netherlands*

²*Max-Planck Institute for Astrophysics, Karl-Schwarzschild-Strasse 1, 85748 Garching, Germany*

ABSTRACT

A substantial fraction of all ionizing photons originate from radiative recombinations. However, in radiative transfer calculations this recombination radiation is often assumed to be absorbed “on-the-spot” because for most methods the computational cost associated with the inclusion of gas elements as sources is prohibitive. We present a new, CPU and memory efficient implementation for the transport of ionizing recombination radiation in the TRAPHIC radiative transfer scheme. TRAPHIC solves the radiative transfer equation by tracing photon packets at the speed of light and in a photon-conserving manner in spatially adaptive smoothed particle hydrodynamics simulations. Our new implementation uses existing features of the TRAPHIC scheme to add recombination radiation at no additional cost in the limit in which the fraction of the simulation box filled with radiation approaches 1. We test the implementation by simulating an HII region in photoionization equilibrium and comparing to reference solutions presented in the literature, finding excellent agreement. We apply our implementation to discuss the evolution of the HII region to equilibrium. We show that the widely used case A and B approximations yield accurate ionization profiles only near the source and near the ionization front, respectively. We also discuss the impact of recombination radiation on the geometry of shadows behind optically thick absorbers. We demonstrate that the shadow region may be completely ionized by the diffuse recombination radiation field and discuss the important role of heating by recombination radiation in the shadow region.

Key words: radiative transfer – methods:numerical – HII regions – galaxies: ISM – diffuse radiation – scattering

1 INTRODUCTION

Many astrophysical problems require a detailed treatment of hydrogen-ionizing radiative transfer (hereafter RT). Examples include the evolution of ionized regions during the epoch of reionization (e.g., Barkana & Loeb 2001; Bolton, Meiksin, & White 2004; Ciardi & Ferrara 2005; Furlanetto, Oh, & Briggs 2006; Mellema et al. 2006; Ilić et al. 2007; Trac & Cen 2007; McQuinn et al. 2007; Wise & Abel 2008; Aubert & Teyssier 2010; Zaroubi 2013; Norman et al. 2013), the transport of stellar radiation through the (dusty) inter-stellar medium (e.g., Ferland et al. 1998; Devriendt et al. 1999; Groves et al. 2008; Jonsson et al. 2010) and its impact on the distribution and morphology of the interstellar gas (e.g., Mellema et al. 2006; Susa 2008; Gritschneider et al. 2010;

Walch et al. 2013), photoevaporation feedback in galaxy formation (e.g., Shapiro, Giroux, & Babul 1994; Gnedin 2000; Dijkstra et al. 2004; Okamoto et al. 2008; Pawlik & Schaye 2009; Petkova & Springel 2011; Finlator, Davé, & Oumlzel 2011; Hasegawa & Semelin 2013), the properties of neutral hydrogen absorbers exposed to the extra-galactic UV background (e.g., Miralda-Escudé 2003; McQuinn et al. 2011; Altay et al. 2011; Yajima, Choi, & Nagamine 2012; Altay et al. 2013; Rahmati et al. 2013a,b), and others. However, radiative transfer is an expensive operation, especially because most methods used to transport ionizing radiation in simulations require a computational cost that scales with the number of sources (see, e.g., the review of reionization simulation methods by Trac & Gnedin 2009, or Mackey 2012). This renders large simulations containing many sources computationally challenging.

Apart from discrete sources of radiation such as stars or accreting black holes, about 40% of the recombinations of hydrogen are accompanied by the emission of ionizing pho-

* E-mail: milan.raicevic@strw.leidenuniv.nl

tons, assuming gas of temperature $T = 10^4$ K as is typical of photoionized regions. The presence of this diffuse recombination radiation component greatly increases the number of sources, thus increasing the numerical challenge. To reduce the computational cost associated with recombination radiation, the majority of works in the literature employ the “on-the-spot” approximation (e.g., Spitzer 1978; Osterbrock 1989), which assumes that the ionizing photons produced in recombinations are absorbed locally, in the immediate surroundings of the recombining parcel of gas. In this approximation, recombination radiation is accounted for by a simple change in the recombination coefficient.

However, the on-the-spot approximation ignores RT effects that may be important. Ritzerveld (2005) showed, using an outward-only analytic approximation, that the intensity of the diffuse recombination radiation should dominate over that of the direct stellar radiation near the ionization fronts (henceforth I-fronts) of HII regions in ionization equilibrium, finding a diffuse-to-source intensity ratio substantially larger than implied by the on-the-spot approximation (for an early discussion see Rubin 1968). Williams & Henney (2009) revisited this issue by carrying out accurate numerical RT simulations of HII regions in ionization equilibrium. They confirmed the picture provided by Ritzerveld (2005) qualitatively, but showed that the outward-only approximation underestimates the contribution of recombination radiation to the total intensity near the source and overestimates it near the I-front, and also discussed the dependence of the diffuse-to-source intensity ratio on the radiation spectrum. Similar recent investigations into the impact of ionization by recombination radiation on the intensity distribution or ionization balance inside HII regions include Hasegawa & Umemura (2010), Cantalupo & Porciani (2011) and Friedrich et al. (2012).

Recombination radiation may strongly affect the morphology of shadows cast by optically thick absorbers. Canto et al. (1998), using an approximate analytic RT model of an optically thick clump illuminated by a central source in a stellar HII region, showed that recombination radiation may highly ionize and photoheat the gas inside the shadow. In their simulations, the dynamical reaction induced by the difference in the temperatures of the gas in- and outside the shadow increases the gas densities until pressure equilibrium is reached, possibly rendering the shadow observable in H α against the HII region. Shadowing by optically thick clumps was also investigated in Razoumov & Scott (1999) using three-dimensional RT and in Pavlakis et al. (2001) using an approximate, inward-only RT scheme coupled to a two-dimensional hydrodynamical simulation, and both these works confirmed that recombination radiation can strongly impact the shadow morphology (see also Hasegawa & Umemura 2010; Rosdahl et al. 2013). On the other hand, Raga et al. (2009), who modeled the “finger” structures in the Carina Nebula as overlapping shadow regions behind multiple clumps of gas using three-dimensional radiation-hydrodynamical simulations, found no significant impact of recombination radiation on the morphology of the simulated nebula.

Other investigations into the role of ionizing recombination radiation on small-scale gaseous structure include Williams (1999), who discussed the potentially inhibiting impact of recombination radiation on the growth

of I-front instabilities (see also Whalen & Norman 2008). Motoyama et al. (2007) simulated the compression of gas clumps exposed to diffuse radiation emitted by the surrounding gas. Adopting a directed, non-isotropic approximation for the RT of diffuse radiation, they showed that recombination photons can photoheat and compress the gas in the clump, increasing the rates at which clumps accrete, possibly implying an increase in the luminosities of the emerging protostars. The effects of recombination radiation on star formation triggered by radiation-driven implosion of gas clumps were also investigated in the three-dimensional radiation-hydrodynamics simulations of Haworth & Harries (2012). Ercolano & Gritschneider (2011) approximated the effects of recombination radiation in simulations of turbulent interstellar gas photoionized by a nearby star, finding less dense and less coherent structures and a small reduction in the efficiency with which turbulence is driven with respect to simulations adopting the on-the-spot approximation. Recombination radiation is also generated in shocks accompanying accretion of gas onto galaxies or protostellar jets, where it may affect the evolution of the unshocked gas ahead of the shock (e.g., Kang & Shapiro 1992; Raga et al. 1999; see also Dopita et al. 2011; Wytthe, Mould, & Loeb 2011).

The role of diffuse radiation in the epoch of reionization is largely unexplored. Ciardi et al. (2001) explicitly followed recombination radiation in their Monte Carlo RT simulations of reionization, but did not discuss its impact. Inoue (2010) used an analytic model to show that accounting for the RT of recombination radiation can impact both the escape of ionizing photons from high- z galaxies, and the average energy carried by the escaping radiation. More importantly, they showed that diffuse nebular ionization leaves a clear Lyman “bump” signature in the spectral energy distributions of galaxies that can be used to characterize the properties of stellar populations in star-forming galaxies.

Rahmati et al. (2013a,b) used the RT technique described in this paper to investigate how ionizing radiation from stars in galaxies and from the UV background shapes the distribution of neutral hydrogen absorbers in and near galaxies in the post-reionization era. They found that the recombination radiation intensity dominates over the UV background intensity in galaxies near densities $n_{\text{H}} \sim 10^{-2} \text{cm}^{-3}$ above which hydrogen starts to self-shield, helping the UV background photons to penetrate to somewhat higher densities. Even in the presence of ionization by local stellar sources, which typically dominate the intensity in the interstellar gas, recombination radiation may dominate the intensity near the densities at which the gas self-shields from the UV background.

In this paper, we present a new implementation of recombination radiation in the RT scheme TRAPHIC (Pawlik & Schaye 2008, 2011). The key idea of this implementation is to reuse the original features of the TRAPHIC code to add the treatment of recombination radiation at almost no additional computational cost in the limit when the maximum number¹ of photon packets is present in the box. This is the relevant limit for the intended use of TRAPHIC

¹ The number of photon packets present in the simulation box has a maximum value in TRAPHIC, which depends on the angular

in, e.g., simulations of galaxy formation close to and after the end of reionization. Away from this limit, the new implementation can still be significantly more computationally efficient than the original implementation described in Pawlik & Schaye (2008, their Section 4.3.2), in which the recombination radiation was emitted using the same framework as used for the emission of stellar radiation.

The paper is structured as follows. In Section 2.1, we present a brief overview of the TRAPHIC method. In Section 2.2, we describe our new implementation of recombination radiation. In Section 3, we apply our implementation in Test 1 of Iliev et al. (2006) and we compare our results to the analytic solution of Ritzerveld (2005) and the numerical solution by Williams & Henney (2009). In Section 4, we use our method to investigate the role of recombination radiation in the shadowing by an absorber near a UV radiation source. This problem is similar in spirit to that studied by, e.g., Canto et al. (1998), Razoumov & Scott (1999), and Rosdahl et al. (2013). Finally, we conclude in Section 5.

2 METHOD

In this section, we provide a concise overview of the TRAPHIC method and the implementation of recombination radiation.

2.1 TRAPHIC: TRANsport of PHotons In Cones

TRAPHIC is a photon packet-based multi-frequency RT scheme designed to transport radiation in smoothed particle hydrodynamics (hereafter SPH) simulations. It is implemented in GADGET (last described in Springel 2005). The scheme itself was presented in Pawlik & Schaye (2008, 2011), and later applied in post-processing by Rahmati et al. (2013a,b) and in radiation-hydrodynamical simulations by Pawlik et al. (2013). TRAPHIC solves the time-dependent RT equation in an explicitly photon-conserving manner by tracing photon packets at the speed of light from the sources through the simulation box. Packets are traced directly on the SPH particles, thus utilizing the full dynamic range of the density field. A key feature of the method is the directional merging of photon packets inside cones, which limits the maximum number of photon packets traced and renders the computational cost of TRAPHIC independent of the number of radiation sources.

The RT calculation proceeds in 2 steps: the radiation transport step and the chemistry step. During the RT step of duration Δt , photons are propagated and absorbed by the gas. During the chemistry step, the absorptions are used to update the species fractions over the same duration Δt . The associated photoheating and radiative cooling is also taken into account. Particles that are sources of radiation emit new photon packets isotropically in N_{EC} directions, where N_{EC} , the “number of emission cones”, is a parameter chosen to obtain converged results. The emission is done in steps² of

resolution at which photon packets are merged. See Section 2.1 for more details.

² This decoupling of the radiative transfer and emission steps is a new feature that has not been described in Pawlik & Schaye 2008. It enables additional control of the angular sampling of the

$\Delta t_{\text{em}} \leq \Delta t$. Before each emission, the isotropic directions are randomly rotated to increase the fraction of the simulation box sampled with photons.

Each source in TRAPHIC can have an arbitrary spectrum, defined by a number of bins at discrete frequencies, N_{freq} . Each photon packet carries photons in a single frequency bin and hence the total number of packets emitted by a source in an emission time step is $N_{\text{EC}} \times N_{\text{freq}}$. The spectral shape within each bin is encoded in the form of a grey absorption cross-section computed by averaging the frequency-dependent absorption cross-section weighted by the source spectrum. This so-called grey approximation is accurate in the optically thin limit, when spectral hardening within each bin is negligible (e.g., Osterbrock 1989).

The newly emitted photons, together with any photons already present in the box, are then propagated forward. In each forward step, photon packets search for neighbours j within the smoothing volume of SPH particle i they are attached to. A given photon packet is then distributed among the neighbours found in the regular cone with opening solid angle of $4\pi/N_{\text{TC}}$ centred on the packet’s propagation direction. The parameter N_{TC} , called the “number of transmission cones”, sets the angular resolution of the transport. The distance l_{ij} , which is the distance to neighbour j projected onto the direction of propagation, is used to compute the optical depth of the absorbing species k (where k is HI, HeI or HeII) using $\tau_{ij,\nu}^k = \langle \sigma_k \rangle_\nu n_j^k l_{ij}$, where $\langle \sigma_k \rangle_\nu$ is the grey cross-section for absorption of the photon packet in frequency bin ν by species k and n_j^k the number density.

The optical depth gives the number of photons absorbed by the gas along the travel length, $\mathcal{N}_{\text{abs},\nu} = \mathcal{N}_{\text{in},\nu} [1 - \exp(-\tau_{ij,\nu})]$, where $\mathcal{N}_{\text{in},\nu}$ is the number of photons in the packet before the transport step and $\tau_{ij,\nu} = \sum_k \tau_{ij,\nu}^k$. Within each RT time step Δt , photon packets are moved until they reach the distance set by the speed of light, $c\Delta t$, i.e., they generally experience several forward propagations and move across multiple inter-particle distances in one transport step. The distance covered is measured by a *clock* associated with each photon packet, and which is initialized upon emission using the time at the beginning of the current RT time step. Corrections due to relativistic effects, which we ignore, are negligible in the applications discussed in this work.

It is possible that a photon packet does not find any neighbours in its transmission cone. In that case, a so-called virtual particle is created randomly within the volume of the transmission cone. The properties of the virtual particle are obtained by SPH interpolation from its SPH neighbours. Its role is to enable the transport of photons in directions without SPH neighbours, after which it is deleted. All absorptions that happen during the transport of photon packets to a virtual particle are distributed among its SPH neighbours and contribute to their ionization and thermal evolution.

Multiple photon packets can arrive at the same SPH particle in one transport step. Then, packets are merged according to their incoming direction, as illustrated in Figure 1. This is achieved by defining a number of isotropic directions, N_{RC} , that define directional bins called reception cones. These reception bins are shown as green cones

volume around sources independent of the size of the RT time step Δt and the number of emission cones N_{EC} .

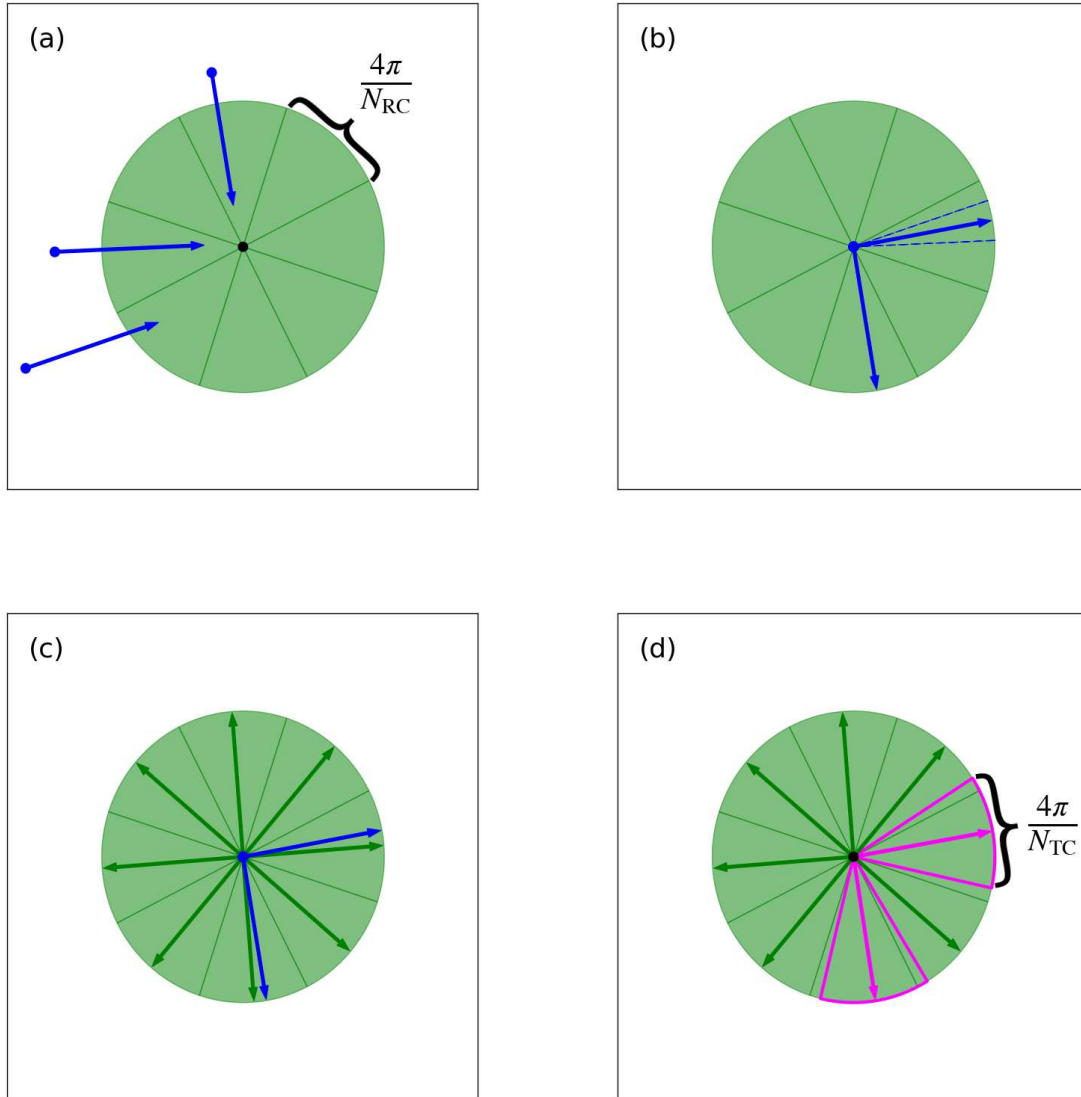


Figure 1. The emission of recombination photons in the new implementation discussed here. The diagrams are a two-dimensional representation of the three-dimensional, 4π solid angle around particles. (a) An SPH particle (black dot) has a set of isotropically directed reception cones attached to it (green cones). Photon packets (blue arrows) arriving at this particle are grouped according to their incoming directions using the reception cones. (b) All packets whose propagation directions fall in the same reception cone are merged into one packet. The direction of the merged packet is set to the luminosity-weighted average of the parent directions. Blue dashed lines show the direction of parent photons before merging, for reference. (c) The isotropic directions that define the reception cones are used to emit recombination radiation from the particle (green arrows). (d) The newly generated recombination radiation packets are instantly merged with existing photons present at the SPH particle (magenta arrows). Note that, for visualization, we assumed that the luminosity of pre-existing photons (blue arrows) is much higher than that of the newly emitted ones (green arrows), causing the directions of merged packets (magenta arrows) to nearly coincide with the blue arrows; we furthermore chose $N_{TC} = N_{RC}$, making the indicated opening angles of the cones in panels (a) and (d) equal in size.

in Figure 1. Each photon packet is sorted in one of these bins according to its direction (top left panel). Photon packets whose propagation directions fall into the same bin are combined into a single new photon packet. The propagation direction of this new, merged photon packet is set to a luminosity-weighted average of the propagation directions of the progenitor packets (top right panel). The reception

directions are frequently rotated to avoid geometrical artifacts. The merging of photons is done separately for each frequency bin. This prevents the mixing of photons from different bins, which enables an accurate tracking of the contribution of individual spectral components to the total intensity. Thanks to this merging procedure, the number of photon packets in the computational volume is at most

$N_{\text{RC}} \times N_{\text{SPH}} \times N_{\text{freq}}$, where N_{SPH} is the number of SPH particles. The computational cost of simulations with TRAPHIC is thus independent of the number of sources.

Once the transport step has completed, the ionization state and thermal energy are updated. The total number of absorptions at each SPH particle is used to estimate the rate of ionizations by photons in frequency bin ν for species k , $\Gamma_{\gamma k, \nu} = \frac{N_{\text{abs, tot, } k, \nu}}{N_k \Delta t}$, where $N_{\text{abs, tot, } k, \nu}$ is the sum of all photon packets in frequency bin ν absorbed by species k within the time step Δt and N_k is the number of atoms of species k in the SPH particle. The total photoionization rate is then the sum of the contributions from all frequency bins. Currently implemented species are HI, HeI and HeII. The associated photoheating rate due to ionizations of each species by photons in frequency bin ν is $\mathcal{H}_{\gamma k, \nu} = \Gamma_{\gamma k, \nu} \langle \epsilon_k \rangle_{\nu}$, where $\langle \epsilon_k \rangle_{\nu}$ is the grey excess heating energy per ionization of species k in frequency bin ν , computed as described in Pawlik & Schaye (2011, here we adopt their optically thin limit). Once the photoionization and photoheating rates have been obtained, they are used to compute the change in the ionization state and temperature during the time step Δt . For details on our method for solving the chemistry equations, see Pawlik & Schaye (2011).

We use the fits to the recombination rate coefficients by Hui & Gnedin (1997). We account for collisional ionization and radiative cooling by collisional ionization/excitation, emission of free-free and recombination radiation and Compton radiation off the CMB using the rates described in Pawlik & Schaye (2011, their Table 1). Unless mentioned otherwise, we adopt Case B recombination and cooling rates in simulations employing the on-the-spot approximation, and Case A recombination and cooling rates when recombination radiation is explicitly followed using RT. Expressions for the frequency-dependent photoionization cross-sections are taken from Verner et al. (1996). Photoionizations are computed in the nebular approximation, i.e., assuming that the electrons in the hydrogen atoms are in the ground state when photoionizations occur, and hence require photon energies of at least 13.6 eV to be freed (e.g., Osterbrock 1989).

Emitting a finite number of photon packets in a finite number of directions may imprint noise in the ionization and temperature fields, as known from simulations with classical Monte Carlo radiative transfer codes. The merging of photon packets may amplify this noise. In simulations with TRAPHIC, numerical noise caused by the Monte Carlo nature of the emission of photons and by the merging is controlled by numerical parameters whose values can be informed by convergence tests. We have presented such tests in Pawlik & Schaye (2008), and we discuss convergence of our results in the current simulations in Appendix A. In radiation-hydrodynamical simulations, Monte Carlo noise may cause artificial pressure differences that affect the dynamics of the gas. Such differences are also controlled by the numerical parameters and can be reduced to have a negligible effect (see, e.g., the discussion in Iliev et al. 2009). However, in this work we consider only the transport of photons on static density fields.

2.2 Implementation of recombination radiation

In this section, we introduce the new implementation of hydrogen recombination radiation in TRAPHIC and discuss the differences relative to the original implementation presented in Pawlik & Schaye (2008, their Section 4.3.2). Note that we had not previously described the results of our tests of the transport of recombination radiation in TRAPHIC, but we already included the transport of diffuse photons (using the new implementation described here) in some of our previous works (Rahmati et al. 2013a,b).

Recombination is the inverse process of photoionization, during which a free electron is captured by an ion into an atomic energy level l . This is followed by the emission of a recombination photon with energy corresponding to the difference between the energy of the atomic level and that of the electron before recombination. The energy of the emitted photon can in some cases be sufficient to cause another photoionization event. In this paper, we focus on accounting for the ionizing recombination radiation in a hydrogen-only medium. In general, the balance between photoionizations and recombinations is governed by the Milne relations (e.g., Rybicki & Lightman 1986). These relations can be used to compute the probability of electron capture to an atomic energy level l , taking into consideration the thermal distribution of the electrons. The total temperature-dependent rate of recombinations is obtained by integrating over captures to *all* atomic energy levels. This rate is often referred to in the literature as the *case A* recombination rate, $\alpha_A(T)$ (e.g. Spitzer 1978). The recombinations to the ground level $l = 1$, occurring at a rate $\alpha_1(T)$, are guaranteed to generate hydrogen-ionizing photons.

In a RT simulation, explicitly following these photons generally represents a significant addition to the computation cost, as each recombining ion becomes a new isotropic source of radiation. To avoid this additional cost, the “on-the-spot” approximation was introduced (e.g. Spitzer 1978; Osterbrock 1989), which assumes that the optical depth of the region around the recombining gas is high enough to absorb all the ionizing recombination photons locally. This is implemented by excluding recombinations to the ground state from the total recombination rate, introducing the *case B* recombination rate, $\alpha_B = \alpha_A - \alpha_1$. Both case A and case B recombination rates can be appropriate substitutes for the explicit RT of recombination radiation in some regimes, but not in general, as we will demonstrate in the next section (Figure 2).

In the original implementation described in Pawlik & Schaye (2008), the emission of recombination radiation was done using the same procedure as used for the emission of photons from stars. That is, an additional set of N_{EC} isotropic emission cones was defined for each SPH particle. The N_{EC} photon packets emitted in these cones were stored on the emitter particle *separately* from any other packets already present. In order to avoid the additional memory and CPU cost associated with introducing additional emission cones to SPH particles, our new implementation *reuses* the N_{RC} reception cones, which are already in place, to emit photons³. This is done

³ The same procedure was used by Rahmati et al. (2013b) to emit radiation from star-forming SPH particles.

by adding the recombination radiation isotropically into the reception cones at the end of each chemistry step Δt (once the recombination radiation luminosity for that step is known), instantly merging with any photons packets already present (see Figure 1). The clocks used to propagate the photon packets at the speed of light are initialized using the time at the beginning of the next RT time step.

The efficiency of the new implementation comes from the fact that almost nothing was added to the TRAPHIC scheme to accomplish the emission of recombination radiation, as the employed reception cones already exist and the memory to store them has already been allocated. The emission in reception cones differs from the emission using emission cones in two respects: the solid angle subtended by the cones ($4\pi/N_{\text{RC}}$ instead of $4\pi/N_{\text{EC}}$) and the frequency with which the cones are rotated. Moreover, in the current work, the emission of recombination photons is done on the chemistry update time step, Δt . This contrasts with the emission of stellar photons and the emission of recombination radiation in the original implementation, which was done on time steps of size $\Delta t_{\text{em}} \leq \Delta t$. The recombination radiation is therefore typically emitted in fewer directions in the new implementation. The coarser angular sampling is, however, offset by the large number of sources of recombination radiation (all SPH particles are potential sources of recombination radiation). Indeed, our tests show fast convergence even for small values of N_{RC} (Appendix A). Comparing simulations using the new and original implementations yields nearly identical results.

A further improvement in memory efficiency can be made by using the same frequency bins for transporting both stellar and recombination radiation. The HI ionizing recombination radiation spectrum is strongly peaked at the Lyman continuum limit, i.e., at energies $\gtrsim 13.6$ eV (e.g., Canto et al. 1998). The spectrum of massive stars also features a significant number of photons close to the Lyman limit, thus a frequency bin around 13.6 eV is necessary to accurately represent it, possibly complemented by additional frequency bins at higher energies. If that frequency bin is also used to transport recombination radiation, the addition of recombination radiation implies practically no extra cost. However, this is not the approach we take in this paper. It is only appropriate if the stellar spectrum in the frequency bin and the spectrum of the recombination radiation are similar. The general case would require to average the cross-sections for the absorption of stellar and recombination photons upon merging of photons in the same frequency bin. In all tests presented in this paper, the recombination radiation is transported in a single frequency bin physically separate from, though overlapping in frequency with, the bin used to transport direct stellar radiation. This allows us to determine unambiguously the contribution of recombination radiation to the total intensity.

In this work we present simulations of the transfer of recombination radiation on static hydrogen-only density fields. We thus do not consider the emission and absorption of helium recombination radiation and the associated ionization and heating in this work (e.g., Cantalupo & Porciani 2011; Friedrich et al. 2012). In some simulations, we also follow the associated photoheating of the gas. The excess energy injected upon absorption of hydrogen recombination photons available to heat the gas is set following Canto et al. (1998)

to $\epsilon_{\text{HI,RR}} = kT$, where T is the temperature of the gas emitting recombination radiation. This assumes that the spectrum of recombination radiation is proportional to $e^{-h\nu/kT}$. However, we ignore the spectral distribution of the recombination radiation when evaluating the grey cross-section for absorption by neutral hydrogen atoms. Throughout this work, we adopt a grey photoionization cross-section for recombination radiation of $\langle\sigma_{\text{HI}}\rangle = 6.3 \times 10^{-18}$ cm² appropriate for monochromatic photons of energy 13.6 eV. We opt for this approximation, which does not affect our general conclusions, because it facilitates the quantitative comparisons with previous works in Section 3.

3 THE ROLE OF DIFFUSE RADIATION IN A STROMGREN SPHERE

In this section, we test our new recombination radiation implementation by comparing results from a simulation of an HII region with analytical and numerical results found in the literature. Specifically, we compare the intensity distribution when the HII region reaches equilibrium (“Stromgren sphere”, Strömberg 1939) to the analytical solution of Ritzerveld (2005) that assumes all transport is directed outwards, and to the numerical RT equation solution of Williams & Henney (2009). We begin by discussing the evolution of the HII region as its I-front expands to reach the Stromgren radius. We will compare the run with accurate RT of recombination radiation to two runs employing two widely used approximations, case A and B.

The simulation setup is as follows. We adopt the same parameters as in Test 1 of the RT Code Comparison project (Iliev et al. 2006). The simulation box is cubic with linear size $L_{\text{box}} = 13.2$ kpc. It is filled with only hydrogen of uniform number density $n_{\text{H}} = 10^{-3}$ cm⁻³, which is initially neutral and has a constant temperature $T = 10^4$ K throughout the simulation. At the center of the box is a single star particle emitting $\dot{N}_{\gamma} = 5 \times 10^{48}$ ionizing photons/s. We transport the stellar radiation using a single frequency bin, assuming monochromatic photons with energy 13.6 eV and an absorption cross-section of $\langle\sigma_{\text{HI}}\rangle = 6.3 \times 10^{-18}$ cm². This differs from the test description in Iliev et al. (2006), who assumed a black body spectrum with temperature $T = 10^5$ K, but facilitates the comparison with the equilibrium solutions presented in Ritzerveld (2005) and Williams & Henney (2009). The hydrogen gas is discretised using 128^3 SPH particles. At each emission time step of size $\Delta t_{\text{em}} = 0.01$ Myr, the star emits $N_{\text{EC}} = 8$ photon packets that are subsequently transported at angular resolution $N_{\text{TC}} = 8$. Photons are merged using $N_{\text{RC}} = 8$ reception cones per particle. Note that the parameter N_{RC} also sets the number of directions in which each gas particle emits recombination photons. The RT time step is set to $\Delta t = 0.1$ Myr. The latter time step is also used to emit recombination photons. We discuss the convergence of our simulation with respect to the spatial resolution, the angular resolution and the time step in Appendix A.

Figure 2 shows the radial profiles of the HI fraction (*top*) and radiation intensity I (*bottom*) during the evolution of the HII region. The columns show our results at three characteristic times, from the initial to the equilibrium state of the HII region. The time is quoted in units of the recombination time, $t_{\text{rec}} = (\alpha_{\text{B}} n_{\text{H}})^{-1} \approx 122.4$ Myr, where α_{B} is

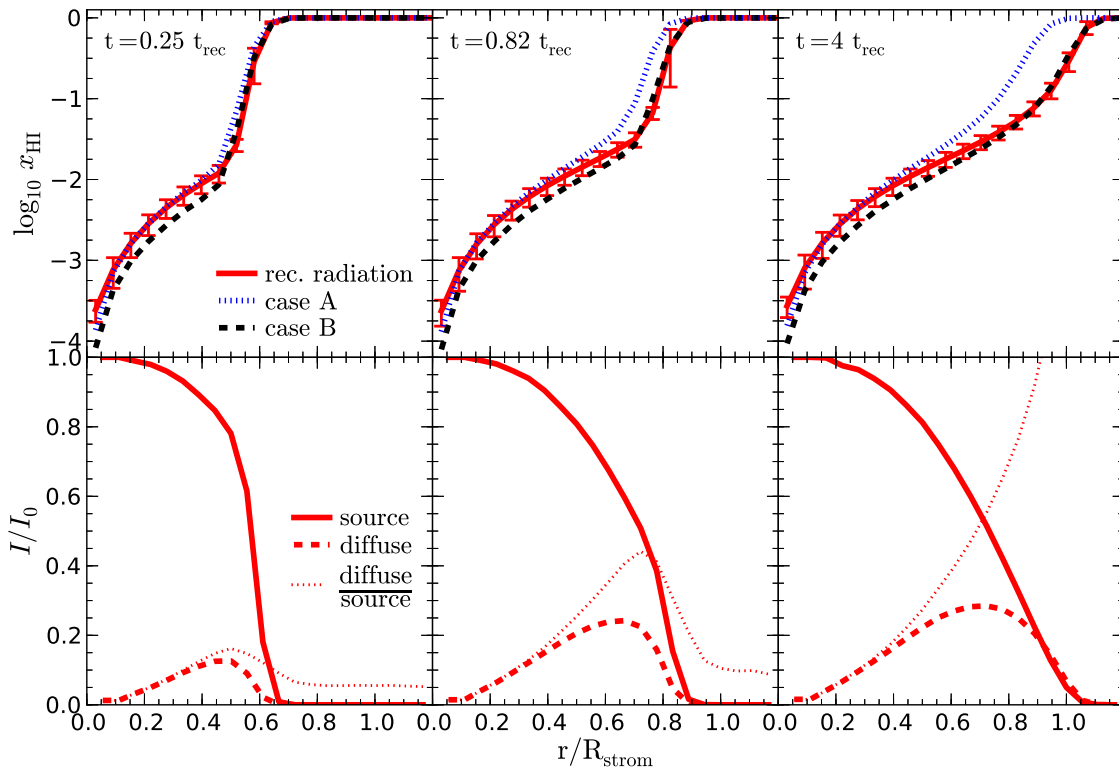


Figure 2. Evolution of the HII region in Test 1 of the Code Comparison project (Iliev et al. 2006), comparing different treatments of recombination radiation. *Top:* The radial profile of the neutral fraction x_{HI} at three different times, quoted in units of the recombination time, $t_{\text{rec}} = 122.4$ Myr. The solution obtained using accurate RT of recombination photons (red solid curve) is compared to the solutions obtained using case A (blue dotted curve) and case B (black dashed curve) recombination coefficients and ignoring the transport of recombination radiation. The RT solution accurately interpolates between the optically thin and thick regimes. *Bottom:* The local radiation intensity I multiplied by $4\pi r^2$, measured in thin spherical shells as described in the text, in units of I_0 , the number of photons emitted per unit time by the source. Contributions to the intensity from the source (red solid curve) and from diffuse recombination radiation (red dashed curve) are shown separately, together with the diffuse-to-source intensity ratio (thin red dotted curve). When the HII region has reached the equilibrium state, the diffuse component dominates the intensity near the I-front (bottom right panel).

the case B hydrogen recombination rate coefficient. We compare the evolution of the HI fraction in the simulation with explicit RT of recombination radiation (red solid curve) to the corresponding evolution in simulations employing the case A (blue dotted curve) and case B (black dashed curve) approximations.

The run with the explicit RT of recombination radiation bridges the results obtained using case A and B recombination rates. In the inner part of the HII region, near the source, where the gas is already highly ionized and has reached ionization equilibrium, the recombination radiation RT result agrees with the case A one, while case B yields a neutral fraction that is too low by a factor $\alpha_{\text{B}}/\alpha_{\text{A}} \approx 0.6$. The origin of the discrepancy with case B is the assumption that the ionizing recombination photons are absorbed on the spot, which is not appropriate in the highly ionized low-density gas that is optically thin to ionizing radiation and from which the majority of the recombination photons should escape. The latter is assumed in case A, which therefore provides a good match to the RT result.

On the other hand, around the I-front where the gas is optically thick and the on-the-spot approximation appropriate, the RT result approaches the case B one, while case A

yields an I-front with a smaller radius (which we define as the radius at which the neutral fraction is $x_{\text{HI}} = 0.5$, following Iliev et al. 2006). The reason for the smaller radius of the I-front in the case A run is that case A assumes that all recombination photons escape. While this assumption is appropriate in optically thin regions, in optically thick regions it leads to a violation of photon conservation and results in a smaller I-front radius. The RT run correctly treats the ionization state in both the optically thin and optically thick regions, meaning it accurately interpolates between the two opacity regimes. A similar discussion but focusing on the equilibrium solution was presented in Cantalupo & Porciani (2011).

The bottom panels in Fig. 2 show the radial profiles of the intensity, separated in contributions from photons emitted by the source (black solid curves) and from recombinations (diffuse component, red dashed curve). We measured the intensity by recording the total number of photons passing through each SPH particle during a RT time step Δt and dividing by this time step. Next, we sum these numbers in thin spherical shells centered on the central source. This yields the total number of photons passing per unit time through a spherical surface with ra-

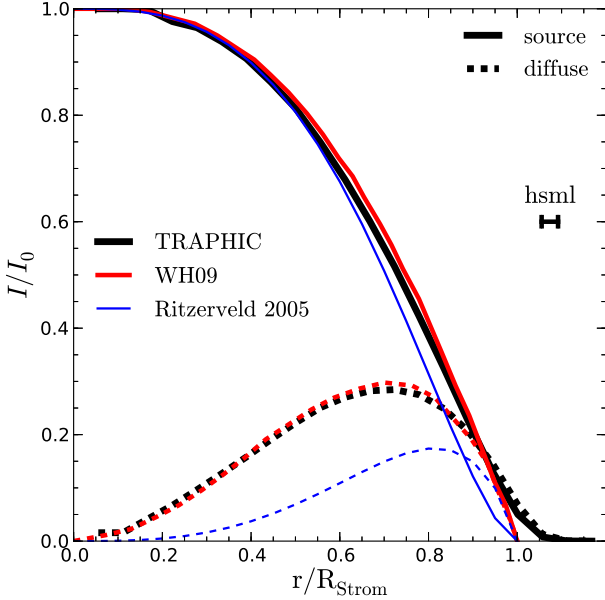


Figure 3. Equilibrium intensity profile. The profile obtained using TRAPHIC (black curves; identical to the corresponding curves in the bottom right panel of Figure 2 computed at $t = 4t_{\text{rec}}$) is compared to an approximate analytic solution (Ritzerveld 2005, blue curves) and a numerical solution using an equilibrium solver (red curves, Williams & Henney 2009). Our solution provides an excellent match to the numerical reference solution, with only small differences at the I-front that can be explained by the lower spatial resolution adopted here (the average radius of the SPH kernels is shown by the bar denoted “hsm1”). The analytic solution assumes outward-only transport of the recombination radiation, which explains why it underestimates the diffuse-to-source intensity ratio near the source and overestimates it near the I-front.

dius r , i.e., $4\pi r^2 I(r)$, which is the quantity discussed in Williams & Henney (2009) and Ritzerveld (2005). The profiles are normalized by dividing by the total number of photons emitted by the source per RT time step, I_0 . The contribution of recombination radiation to the total intensity increases with time. In the early stages of HII region growth, i.e., at times $t \ll t_{\text{rec}}$ (bottom left panel), the contribution of recombination radiation is sub-dominant, reaching at most $\sim 15\%$ of the source intensity at any given radius. As the time approaches one recombination time, the diffuse intensity contributes significantly to the total, reaching up to $\sim 40\%$ of the source intensity near the I-front. Finally, in equilibrium, i.e., at times $t \gg t_{\text{rec}}$ (bottom right panel), the recombination radiation intensity starts to dominate over the stellar intensity near the I-front. Note for comparison that the Case B approximation yields a ratio of diffuse and source intensity of about 0.6 independent of the distance from the source, assuming that the cross-sections for absorption of diffuse and source radiation are equal (Williams & Henney 2009). Our simulations show that case B overestimates the diffuse intensity significantly at early times or near the source, and underestimates it at late times near the I-front.

The equilibrium state of the HII region has been the

standard test of implementations of recombination radiation in the literature, with solutions provided both analytically and numerically. In Figure 3, we compare our equilibrium result (black curves) with two such works: the analytic approximation of Ritzerveld (2005) (blue curves) and the numerical solution of Williams & Henney (2009) (red curves). Ritzerveld (2005) provides an analytic approximation for the equilibrium state of a spherical HII region by assuming that all recombination photons are transported radially away from the source. This *outward approximation* simplifies the solution of the RT equation greatly as the isotropic source term of recombination radiation disappears. However, as shown by our simulations, the outward approximation results in a radial distribution of the diffuse intensity that is very different from that in the RT simulation. As already discussed in Williams & Henney (2009), the diffuse intensity near the source is significantly lower than in the RT solution as all recombination photons are assumed to go straight towards the edge of the HII region. As a consequence, the outward-only approximation underestimates the diffuse-to-total intensity ratio near the source and overestimates it near the I-front.

Williams & Henney (2009) computed the distribution of diffuse and source intensity in stellar HII regions using the method of discrete ordinates (e.g. Hummer & Seaton 1963; Rubin 1968) which allows for the accurate integration of the RT equation including the recombination radiation source term. Compared to the Ritzerveld (2005) approach, the Williams & Henney (2009) calculation shows a recombination intensity larger by a factor of about 2 near the source, while still finding it to dominate close to the I-front. The results of our RT simulation (black curves in Fig. 3) are in excellent agreement with the results of Williams & Henney (2009) across the full range of radii⁴. Small differences exist near the far edge of the I-front, where in our method radiation penetrates slightly further away from the source. These differences are caused by the limited resolution adopted in our simulation (the I-front position is slightly pushed forward due to SPH kernel smoothing).

In conclusion, our new non-equilibrium implementation of recombination radiation in TRAPHIC yields an equilibrium intensity profile that is in excellent agreement with the accurate numerical equilibrium solution of Williams & Henney (2009). For $r \ll R_{\text{strom}}$, direct source photons dominate the intensity and the ionization balance is close to that assuming case A. On the other hand, at $r \approx R_{\text{strom}}$, diffuse recombination photons dominate the intensity and the ionization balance is close to that assuming case B. Away from these two limiting recombination regimes, the accurate computation of the ionization balance

⁴ The setup of our simulations assumes a hydrogen number density and source luminosity different from those used in Williams & Henney (2009). Thus, the comparison is only appropriate if the solution is self-similar. In the outward-only approximation discussed in Ritzerveld (2005), this is indeed the case. In their Eqs. 7 and 8, the term in front of the brackets on the right-hand side is the total number of photons emitted by the source per unit time, and therefore the radiation field ratios depend only on the ratio of the distance from the source and the Stromgren radius. We have not explicitly checked the self-similarity of the numerical solution.

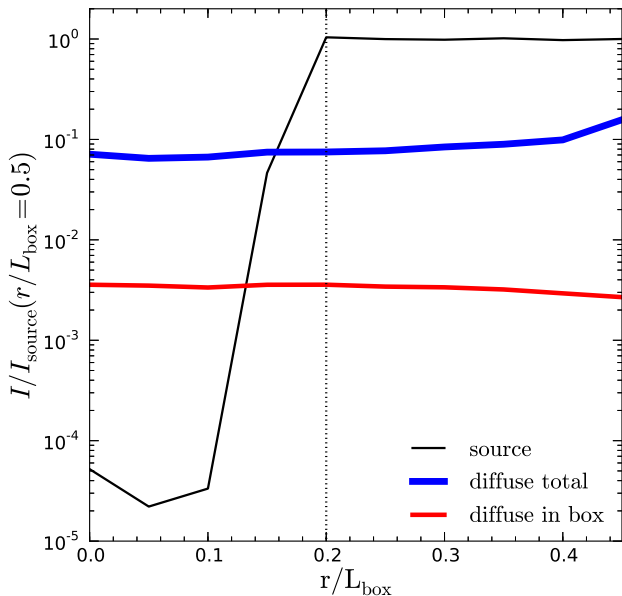


Figure 5. Intensity of different radiation field components averaged in thin cylindrical shells extending radially away from the major axis of the shadow. The intensity is measured after ionization equilibrium has been reached ($t = 3t_{\text{rec}}$). All values are quoted in units of the source radiation intensity averaged in a shell $r = 0.5L_{\text{box}}$ away from the major axis, $I_{\text{source}}(r/L_{\text{box}} = 0.5)$. The source radiation intensity (black solid curve) is constant outside of the shadow region (marked by the vertical thin dotted black curve), while dropping 4 orders of magnitude inside it. On the other hand, the intensity of the diffuse recombination radiation (blue solid curve) is nearly independent of distance to the central axis (red dashed curve). The intensity of recombination radiation is dominated by the contributions originating from outside the box.

requires an explicit treatment of the RT of recombination photons. The accurate computation of the diffuse-to-direct intensity ratio requires RT for all opacity regimes.

4 DIFFUSE RADIATION IN SHADOWED REGIONS

Here, we investigate the impact of recombination radiation on shadows cast by optically thick objects encountered by an I-front. Such shadows are often used to demonstrate the geometric precision of a RT method (e.g. Iliev et al. 2006, 2013). However, most RT methods do not treat the transport of diffuse recombination radiation which can penetrate into the shadow region and, in some cases, completely ionize it. Canto et al. (1998) provided an approximate analytic treatment of recombination radiation in the shadows behind optically thick gas clumps, assuming cylindrical symmetry of the shadow regions. We apply our implementation to a problem similar to the one studied in Canto et al. (1998).

We implemented an artificial disk-shaped radiation barrier and placed it in the path of a plane-parallel I-front entering the box from one side (see Fig. B1). This produces a cylindrical shadow behind the barrier, i.e., a cylindrical re-

gion of lower ionization compared to the unobstructed surroundings. The barrier is artificial in the sense that it is not part of the density field. Instead, for simplicity, it is implemented as a region that instantly removes all photon packets that pass through it. The barrier is a disk with radius $r_{\text{barrier}} = 0.2L_{\text{box}}$ and is placed parallel to the $x = 0$ side of the box at coordinates $(0.27, 0.5, 0.5) \times L_{\text{box}}$.

Our setup assumes that the simulation box is fully ionized by an external source driving a plane-parallel I-front assumed to extend to infinity in the directions perpendicular to the x -axis, the direction of propagation. The implementation of this setup requires us to overcome a practical problem. In short, in order for the source to ionize the box, a sufficiently large external flux must be assumed. The resulting neutral fraction in the non-shadow region then implies a mean free path for ionizing radiation larger than the box size. However, the mean free path dictates the amount of recombination radiation reaching a given point inside the box. When the mean free path is larger than the box, the contribution to the recombination radiation field originating in the ionized gas outside the box has to be added by hand. Here we add this contribution by placing additional sources at the four sides of the box that are parallel to the main axis of the shadow region (see below and Appendix B). Our setup is idealized but ensures that the shadow region can become highly ionized by the diffuse radiation. This facilitates the discussion of the role of heating of the shadow region by recombination photons, which is the focus of this section.

The simulation parameters are as follows: the simulation box is filled with hydrogen-only gas of uniform density $n_{\text{H}} = 10^{-3} \text{ cm}^{-3}$ which is represented using $N_{\text{part}} = 32^3$ SPH particles⁵. The simulation box is cubic with $L_{\text{box}} = 13.2 \text{ kpc}$ and is illuminated by the source, a plane-parallel radiation front⁶ entering the box perpendicular to the $x = 0$ side, with flux $F_{\text{source}} = 10^6 \text{ photons/s/cm}^2$. Plane-parallel source photons, recombination photons emitted inside the box and recombination photons emitted outside the box are transported in separate frequency bins, one bin for each radiation component. Following Iliev et al. (2006), we adopt a black body spectrum with temperature $T = 10^5 \text{ K}$, which is characteristic of massive metal-free stars, the so-called

⁵ The spatial resolution used for the barrier shadowing test is intentionally modest to approximate conditions in spatially adaptive cosmological simulations. In such simulations, most resolution elements are placed in the high density regions that cast the shadows, while the shadow regions are sampled at significantly lower resolution. However, since the density field is uniform and since TRAPHIC is a photon-conserving RT method, our results are insensitive to resolution.

⁶ We use the plane-parallel radiation front implementation described in Rahmati et al. (2013a). The radiation front is produced by placing virtual particles on a regular grid along the box side, with each virtual particle representing a photon packet with a direction perpendicular to the box side. The number of photons in the packets is set to achieve the required flux entering from the simulation side. If the number of virtual particles is not very high (here we used 100^2 particles), SPH particles very close to the box side at which the radiation front emerges can be missed by the transmission cones of the photons, and these then remain neutral. This causes the noise in the neutral fraction field at the left edge of the panels in Figure 4, but has otherwise no consequences, as the number of photons remains conserved.

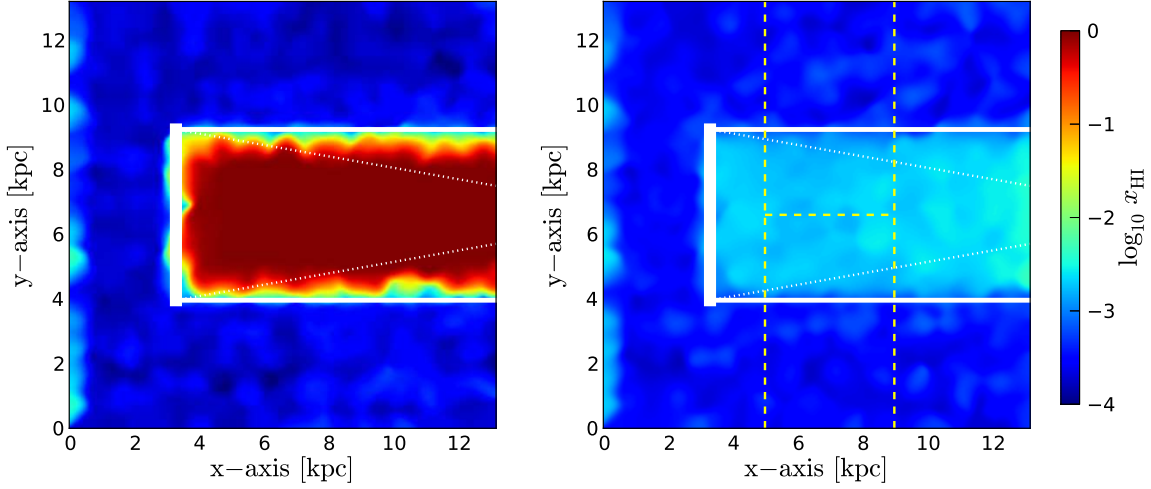


Figure 4. Shadow region behind an artificial barrier, without (*left*) and with (*right*) the RT of diffuse recombination radiation, in the latter case including the contribution of recombination radiation originating from outside the simulation volume. Images show the neutral fraction field in the $z = L_{\text{box}}/2$ plane. The artificial barrier is placed at the center of the $x = 0.27L_{\text{box}}$ plane (thick solid white line). The edges of the shadow in the ideal case are indicated by thin solid white lines, while the formal angular resolution (i.e. half of the opening angle subtended by a transmission cone) is shown using thin white dotted lines. The shadow is much sharper than implied by the formal angular resolution, in agreement with the discussion in Pawlik & Schaye (2008). Thin yellow dashed lines mark the region used to compute the profiles presented in Figures 5 and 6. Without the RT of recombination radiation and adopting the on-the-spot approximation (*left*), the shadow remains neutral, while with it (*right*), it becomes highly ionized. The overlap of the shadow with the barrier is due to the smoothing by the visualization software. The small HI gradient in the back of the shadow region in the right panel is due to the setup not accounting for extra recombination photons originating from beyond the $x = L_{\text{box}}$ side of the box.

Population III. Thus, in contrast to the previous section, in which we assumed that the source photons have energies of 13.6 eV, we adopt the grey cross-section for absorption of the source photons implied by this spectrum, $\langle\sigma_{\text{HI}}\rangle = 1.6 \times 10^{-18} \text{ cm}^2$, and the associated excess photoheating energy $\langle\epsilon_{\text{HI}}\rangle = 6.3 \text{ eV}$ available to heat the gas. The RT time step is set to $\Delta t = 0.1 \text{ Myr}$, and source photons are injected using an emission time step $\Delta t_{\text{em}} = \Delta t$. Photons are transported at an angular resolution of $N_{\text{TC}} = 128$, and merged at an angular resolution of $N_{\text{RC}} = 8$.

The recombination radiation emitted outside the simulation volume is added at the 4 sides of the box that are parallel to the propagation direction of the plane-parallel source wave. At each of the 4 sides, a regular grid of 50^2 boundary particles is created, each emitting recombination radiation isotropically. The recombination luminosity of each boundary particle is determined consistently considering the mean free path implied by the ionized fraction in front of the barrier. Note that we add photons from only 4 out of 6 sides without adjusting the luminosities of the boundary particles to compensate for the implied reduction of photons, i.e., we ignore the recombination radiation emerging from the box sides perpendicular to the central axis of the shadow. However, the precise recombination radiation intensity is unimportant to our discussion as long as the shadow is ionized, because we focus on the role of photoheating in shadows ionized by recombination radiation. The boundary particles only begin radiating after the I-front driven by the external source has passed them. For more details, see Appendix B.

In the following, we present simulations with and without the RT of recombination radiation. In simulations without RT of recombination radiation, the on-the-spot approx-

imation is employed, and the luminosities of the boundary particles are set to zero. We investigate the role of photoionization heating by carrying out simulations that ignore photoheating, simulations that include heating only by direct source photons, and simulations that include heating by both source and recombination photons.

Figure 4 shows the hydrogen neutral fraction in a slice through the center (the $z = L_{\text{box}}/2$ plane) of the simulation box after the equilibrium state has been reached ($t = 3t_{\text{rec}}$, where $t_{\text{rec}} = 122.4 \text{ Myr}$, assuming a temperature $T = 10^4 \text{ K}$). When the on-the-spot approximation is employed, our simulations find a well-defined neutral shadow region behind the barrier, with small edge effects that are consistent with the adopted spatial and angular resolution (left panel). On the other hand, when the on-the-spot approximation is dropped and recombination radiation is treated using RT, the shadow region is highly ionized (right panel). Both runs ignore the heating of the gas by photoionization, assuming a constant temperature $T = 10^4 \text{ K}$ throughout the simulation box. Apart from the sampling noise due to the finite number of SPH particles, there are two numerical artifacts visible in Figure 4. The lower ionization fraction in a thin region near the $x = 0$ plane is caused by some SPH particles being missed by the photon packets driving the plane-parallel ionization front (see footnote 6). The gradient in the HI fraction in the shadow region ionized by recombination radiation in the right panel arises because we do not inject recombination radiation originating from beyond the $x = L_{\text{box}}$ side of the simulation box.

Figure 5 shows the intensity of the individual radiation components. As in Section 3, we measured the intensity by recording the total number of photons passing through each

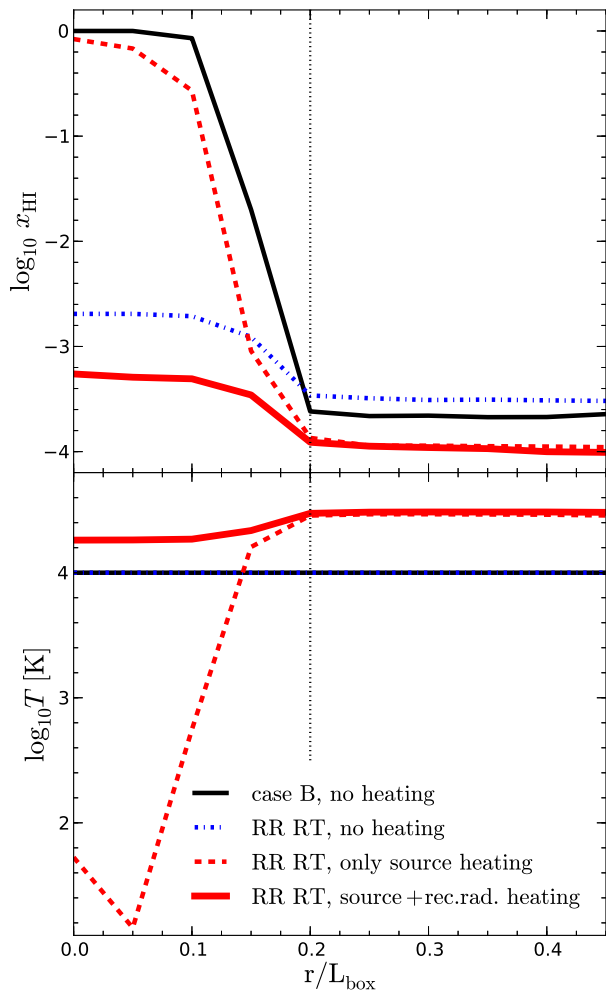


Figure 6. Effect of photoheating. Average HI fraction (*top*) and temperature (*bottom*) in thin cylindrical shells extending radially away from the shadow’s prime axis at $t = 3t_{\text{rec}}$. In the absence of radiation heating (and assuming a constant temperature of 10^4 K), the run adopting the on-the-spot approximation (black solid curve) finds a neutral shadow, whereas the run that follows the propagation of recombination radiation using RT (blue dot-dashed curve) finds the shadow highly ionized. When source photons are allowed to heat the gas (red dashed curve), the shadow region remains at the initial temperature of 10^2 K or even cools slightly below it (bottom panel). The low temperatures imply high recombination rates, leaving the gas mostly neutral (top panel). On the other hand, when also recombination photons are allowed to heat the gas (solid red curve), the shadow region is warm and highly ionized.

SPH particle during a RT time step Δt and dividing by this time step. However, here we average these numbers in thin cylindrical shells centered on the shadow region’s major axis, i.e., the yellow dashed line parallel to the shadow in Figure 4. We construct a series of concentric cylindrical shells starting at this axis and extending radially away from

the major axis of the shadow. The radius of the largest shell is $r = 0.5L_{\text{box}}$. The height of each cylindrical shell is shown in Figure 4 by two vertical yellow dashed lines. The intensities are normalized by dividing by the intensity of source photons averaged in a shell $r = 0.5L_{\text{box}}$ away from the major axis, $I_{\text{source}}(r/L_{\text{box}} = 0.5)$.

Comparing the intensity of recombination radiation emitted in the box (red solid curve) and the total diffuse intensity (blue solid curve) that includes the contribution from photons added to account for the emission of recombination radiation in ionized gas outside of the box, shows that the outside-the-box contribution dominates in this setup. The diffuse recombination radiation intensity is nearly uniform throughout the box while the source intensity vanishes nearly completely within the shadow. The small amount of source radiation in the shadow is caused by the finite angular resolution of TRAPHIC and SPH smoothing. The shadow boundaries are nevertheless much sharper than formally implied by the adopted angular resolution as discussed in Pawlik & Schaye (2008). Moreover, the small amount of radiation is not enough to ionize the gas significantly, as can be seen in the left panel of Fig. 4.

Figure 6 shows the effect of photoionization heating by recombination radiation on the neutral fractions (top) and temperatures (bottom) in the shadow region. The neutral fractions and temperatures were averaged in the same thin cylindrical shells used to compute the intensity shown in Figure 5. The two runs that ignore photoheating, with and without RT of recombination radiation (blue dot-dashed and black solid curves respectively), assume a constant temperature of $T = 10^4$ K. Slices through the simulation box of these two runs were shown in Figure 4. As discussed before, the run adopting the on-the-spot approximation yields completely neutral gas in the shadow region, whereas the other run yields highly ionized gas of neutral hydrogen fraction $x_{\text{HI}} \sim 10^{-3}$. The difference between the neutral fractions in the two runs outside of the shadow region is caused by the difference in the adopted recombination rates: the run without RT of recombination radiation uses the case B rate whereas the one with RT of recombination radiation uses case A.

The other two runs presented in Figure 6 include photoheating in two variants, one assuming that only direct source photons heat the gas (red dashed curve) and the other assuming that both the source and recombination photons heat the gas (solid red curve). Both of these runs utilize the full RT treatment of recombination radiation. In our simulations, direct photons heat the gas outside the shadow to $T_{\text{heat, source}} \approx 27000$ K. This temperature is used to set the excess energy carried by recombination photons, $\epsilon_{\text{HI, RR}} = kT_{\text{heat, source}} \approx 2.3$ eV, available to heat the gas following our discussion in Section 2.2. For simplicity, the excess energy is set at the beginning of the simulations to this value and held constant independent of the actual gas temperatures, which may deviate slightly from the value quoted above. The initial temperature in both of these runs is set to $T_{\text{init}} = 10^2$ K.

The high recombination rate implied by the low initial temperature causes the shadow region in the run without photoheating by recombination radiation (dashed red curve) to remain substantially neutral, in contrast to the same run without any photoheating in which we assumed

a temperature of 10^4 K (blue dot-dashed curve). The very low temperatures < 100 K of the shadow center in the former run are the result of recombination cooling as the gas is mildly ionized by diffuse photons. The cooling is not offset by photoheating, as in this setup recombination radiation is not allowed to heat the gas. As before, the small amount of photoionization and photoheating in the shadow region is caused by the finite spatial and angular resolution that results in the leakage of source photons beyond the shadow boundaries.

Setting the excess energy carried by recombination photons to zero helps to illustrate the case in which recombination radiation ionizes the gas but does not significantly heat it, as may be expected if the recombination radiation spectrum is very soft. On the other hand, if we assume that the spectrum of recombination radiation is set by the temperature of the gas illuminated by a source with a relatively hot blackbody spectrum of 10^5 K (red solid curve), then the shadow region is warm and highly ionized. In many practical situations, the temperatures and ionized fractions of the shadow will likely lie in between these two cases. The run that accounts for photoheating by both direct and recombination radiation yields a much higher temperature than the run that only accounts for photoheating by direct photons and, because of the dependence of the recombination rate on temperature, accordingly finds a much lower neutral fraction.

In this section, though the gas in our simulations was initialized to be neutral and we followed the propagation of the I-front driven by the external source, we focused on the shadow region in photo-ionization equilibrium, i.e., we did not discuss the change in morphology of the shadow during the approach to equilibrium. Canto et al. (1998) showed that, in realistic situations, depending on the strength of the recombination radiation intensity, in equilibrium the shadow region will either be fully ionized or contain a neutral core. However, this does not address the interesting and relevant question for how long shadows behind absorbers manage to persist. Additional and less idealized simulations than those presented here are needed to address this question. As discussed in Williams & Henney (2009), while the diffuse radiation intensity may be a significant fraction of the intensity of direct photons, the lateral flux of diffuse photons into the shadow may be relatively low as the diffuse radiation field may be non-isotropic. Because of these complications, the ability of recombination radiation to ionize shadows will highly depend on the specific problem and may be less strong than found here.

In conclusion, we find that the well-defined dark and cold shadows used to test RT techniques (e.g. Iliev et al. 2006) do not necessarily persist when the on-the-spot approximation is abandoned and the transport of recombination radiation is accurately accounted for. The exact state of the shadowed region will depend on both the intensity and the spectrum of both the direct source photons and the diffuse recombination photons, which may significantly alter the temperatures and the ionization balance inside the shadow region.

5 DISCUSSION

We have presented a new, CPU and memory efficient implementation of ionizing recombination radiation in the TRAPHIC radiative transfer (RT) scheme. The new implementation improves on the original implementation described in Pawlik & Schaye (2008) by re-using features already present in the TRAPHIC scheme. The reception cone directions, used to group photons from similar directions to control the computational cost of the RT with TRAPHIC, are re-used as emission directions for recombination radiation. As in the original implementation, the computational cost is independent of the number of sources thanks to the merging of photon packets with similar directions.

We applied our implementation to two problems. First, in Section 3, we discussed the role of recombination radiation in the evolution of a spherical HII region driven by a central stellar source. We showed, in Figure 2, that, as expected, the widely used case A and case B approximations for the effect of recombination radiation on the ionization balance are only accurate in, respectively, the optically thin and thick regimes and that a detailed treatment of the transport of recombination radiation is required to obtain accurate solutions in more general regimes. The accurate computation of the diffuse-to-source intensity ratio always necessitates an accurate RT treatment of recombination photons. In equilibrium, our results are in excellent agreement with those of Williams & Henney (2009), who employed a numeric RT scheme specifically designed to simulate the effects of recombination radiation in HII regions in equilibrium. We confirm the conclusion of Williams & Henney (2009) that the approximate analytic solution of Ritzerveld (2005), though in qualitative agreement with the numerical RT solution and hence providing a substantial improvement on the commonly employed on-the-spot approximation, underestimates the recombination radiation intensity relative to the source intensity near the source and overestimates it near the I-front.

Second, in Section 4, we investigated the shadowing of ionizing radiation behind optically thick obstacles. In equilibrium, the RT treatment of recombination radiation leads to a highly ionized shadow that is also significantly heated. In Figure 6, we showed that it is important to account self-consistently for the radiative heating by recombination radiation. If photoheating is unimportant, cold gas in the shadow remains substantially neutral even though it is illuminated by the diffuse flux, because low gas temperatures imply high recombination rates. These results, which are consistent with those in earlier works such as Canto et al. (1998), suggest that shadow regions in RT simulations that treat the radiation using the on-the-spot approximation may not resemble real shadows, except perhaps for a brief time just after the onset of irradiation.

This paper focused on the numerical implementation and ignored some physical intricacies associated with recombination radiation. Since hydrogen recombination radiation is strongly peaked near the Lyman limit, any redshifting of the spectrum would make photons unable to ionize hydrogen. If redshifting is caused by cosmological expansion alone, a recombination photon would have to travel $\sim 10^2(T/10^4 \text{ K})(1+z)^{-3/2}$ proper kpc to fall below the Lyman limit, which at $z = 0$ is much larger than the

scales of interest here. However, redshifting (and blueshifting) may become important at much smaller scales at higher redshifts or if peculiar velocities are non-negligible. We have also ignored recombination radiation emitted by helium. The additional complicating factor when helium is included, is that helium recombinations can ionize both hydrogen and helium, requiring special care even when the on-the-spot approximation is used (Cantalupo & Porciani 2011; Friedrich et al. 2012). We further ignored effects of spectral hardening and the absorption of photons by helium and the associated photoheating, both of which can be important (e.g., Maselli, Ciardi, & Kanekar 2009; Pawlik & Schaye 2011; Ciardi et al. 2012)

The new implementation of recombination radiation presented in this paper has already been used by Rahmati et al. (2013a,b) to investigate the effect of ionizing radiation on neutral hydrogen absorbers in the post-reionization era. There, we demonstrated that the presence of recombination radiation smooths the transition between ionized and self-shielded neutral regions. It can also raise the photoionization rate within formally self-shielded regions by several orders of magnitude. This result is a good example of the role of recombination radiation in most common RT problems, usually not dominant but capable of significantly changing the behaviour of the whole system. Thanks to its efficiency, our new implementation enables us to dispense with approximate treatments of the recombination radiation if appropriate.

ACKNOWLEDGMENTS

The simulations presented here were run on the Cosmology Machine at the Institute for Computational Cosmology in Durham (which is part of the DiRAC Facility jointly funded by STFC, the Large Facilities Capital Fund of BIS, and Durham University) as part of the Virgo Consortium research programme. This work was sponsored with financial support from the Netherlands Organization for Scientific Research (NWO), also through a VIDI grant and an NWO open competition grant. We also benefited from funding from NOVA, from the European Research Council under the European Unions Seventh Framework Programme (FP7/2007-2013) / ERC Grant agreement 278594-GasAroundGalaxies and from the Marie Curie Training Network CosmoComp (PITN-GA-2009-238356). AHP receives funding from the European Union's Seventh Framework Programme (FP7/2007-2013) under grant agreement number 301096-proFeSsoR.

REFERENCES

Altay G., Theuns T., Schaye J., Booth C. M., Dalla Vecchia C., 2013, MNRAS, doi:10.1093/mnras/stt1765
 Altay G., Theuns T., Schaye J., Crighton N. H. M., Dalla Vecchia C., 2011, ApJ Letters, 737, L37
 Aubert D., Teyssier R., 2010, ApJ, 724, 244
 Barkana R., Loeb A., 2001, Physics Reports, 349, 125
 Bolton J., Meiksin A., White M., 2004, MNRAS, 348, L43
 Cantalupo S., Porciani C., 2011, MNRAS, 411, 1678

Canto J., Raga A., Steffen W., Shapiro P., 1998, ApJ, 502, 695
 Ciardi B., Ferrara A., 2005, Space Science Reviews, 116, 625
 Ciardi B., Ferrara A., Marri S., Raimondo G., 2001, MNRAS, 324, 381
 Ciardi B., Bolton J. S., Maselli A., Graziani L., 2012, MNRAS, 423, 558
 Devriendt J. E. G., Guiderdoni B., Sadat R., 1999, A&A, 350, 381
 Dijkstra M., Haiman Z., Rees M. J., Weinberg D. H., 2004, ApJ, 601, 666
 Dopita M. A., Krauss L. M., Sutherland R. S., Kobayashi C., Lineweaver C. H., 2011, Ap&SS, 335, 345
 Ercolano B., Gritschneider M., 2011, MNRAS, 413, 401
 Faucher-Giguère C.-A., Lidz A., Zaldarriaga M., Hernquist L., 2009, ApJ, 703, 1416
 Ferland G. J., Korista K. T., Verner D. A., Ferguson J. W., Kingdon J. B., Verner E. M., 1998, Publications of the Astronomical Society of the Pacific, 110, 761
 Ferland G. J., Peterson B. M., Horne K., Welsh W. F., Nahar S. N., 1992, ApJ, 387, 95
 Finlator K., Davé R., Özel F., 2011, ApJ, 743, 169
 Friedrich M. M., Mellema G., Iliev I. T., Shapiro P. R., 2012, MNRAS, 421, 2232
 Furlanetto S. R., Oh S. P., Briggs F. H., 2006, PhR, 433, 181
 Gnedin N. Y., 2000, ApJ, 542, 535
 Gritschneider M., Naab T., Burkert A., Walch S., Heitsch F., Wetzstein M., 2009, MNRAS, 393, 21
 Gritschneider M., Burkert A., Naab T., Walch S., 2010, ApJ, 723, 971
 Groves B., Dopita M. A., Sutherland R. S., Kewley L. J., Fischera J., Leitherer C., Brandl B., van Breugel W., 2008, ApJS, 176, 438
 Hasegawa K., Umemura M., 2010, MNRAS, 407, 2632
 Hasegawa K., Semelin B., 2013, MNRAS, 428, 154
 Haworth T. J., Harries T. J., 2012, MNRAS, 420, 562
 Hui L., Gnedin N. Y., 1997, MNRAS, 292, 27
 Hummer D. G., Seaton M. J., 1963, MNRAS, 125, 437
 Iliev I. T., Ciardi B., Alvarez M. A., Maselli A., Ferrara A., Gnedin N. Y., Mellema G., Nakamoto T., Norman M. L., Razoumov A. O., Rijkhorst E.-J., Ritzerveld J., Shapiro P. R., Susa H., Umemura M., Whalen D. J., 2006, MNRAS, 371, 1057
 Iliev I. T., et al., 2009, MNRAS, 400, 1283
 Iliev I. T., Mellema G., Shapiro P. R., Pen U.-L., 2007, MNRAS, 376, 534
 Inoue A. K., 2010, MNRAS, 401, 1325
 Jonsson P., Groves B. A., Cox T. J., 2010, MNRAS, 403, 17
 Kang H., Shapiro P. R., 1992, ApJ, 386, 432
 Mackey J., 2012, A&A, 539, A147
 Maselli A., Ciardi B., Kanekar A., 2009, MNRAS, 393, 171
 McQuinn M., Lidz A., Zahn O., Dutta S., Hernquist L., Zaldarriaga M., 2007, MNRAS, 377, 1043
 McQuinn M., Oh S. P., Faucher-Giguère C.-A., 2011, ApJ, 743, 82
 Mellema G., Arthur S. J., Henney W. J., Iliev I. T., Shapiro P. R., 2006, ApJ, 647, 397
 Mellema G., Iliev I. T., Pen U.-L., Shapiro P. R., 2006, MNRAS, 372, 679

- Miralda-Escudé J., 2003, *ApJ*, 597, 66
 Motoyama K., Umemoto T., Shang H., 2007, *A&A*, 467, 657
 Norman M. L., Reynolds D. R., So G. C., Harkness R. P., 2013, arXiv, arXiv:1306.0645
 Okamoto T., Gao L., Theuns T., 2008, *MNRAS*, 390, 920
 Osterbrock D. E., 1989, *Astrophysics of gaseous nebulae and active galactic nuclei*
 Pavlakis K. G., Williams R. J. R., Dyson J. E., Falle S. A. E. G., Hartquist T. W., 2001, *A&A*, 369, 263
 Pawlik A. H., Milosavljević M., Bromm V., 2013, *ApJ*, 767, 59
 Pawlik A. H., Schaye J., 2008, *MNRAS*, 389, 651
 Pawlik A. H., Schaye J., 2009, *MNRAS*, 396, L46
 Pawlik A. H., Schaye J., 2011, *MNRAS*, 412, 1943
 Petkova M., Springel V., 2011, *MNRAS*, 412, 935
 Raga A. C., Mellema G., Arthur S. J., Binette L., Ferruit P., Steffen W., 1999, *RMxAA*, 35, 123
 Raga A. C., Henney W., Vasconcelos J., Cerqueira A., Esquivel A., Rodriguez-Gonzalez A., 2009, *MNRAS*, 392, 964
 Rahmati A., Pawlik A. H., Raičević M., Schaye J., 2013a, *MNRAS*, 430, 2427
 Rahmati A., Schaye J., Pawlik A. H., Raičević M., 2013b, *MNRAS*, 431, 2261
 Razoumov A. O., Scott D., 1999, *MNRAS*, 309, 287
 Ritzerveld J., 2005, *A&A*, 439, L23
 Rosdahl J., Blaizot J., Aubert D., Stranex T., Teyssier R., 2013, *MNRAS*, doi:10.1093/mnras/stt1722
 Rubin R. H., 1968, *ApJ*, 153, 761
 Rybicki G. B., Lightman A. P., 1986, *Radiative Processes in Astrophysics*
 Shapiro P. R., Giroux M. L., Babul A., 1994, *ApJ*, 427, 25
 Spitzer L., 1978, *Physical processes in the interstellar medium*
 Springel V., 2005, *MNRAS*, 364, 1105
 Strömgren B., 1939, *ApJ*, 89, 526
 Susa H., 2008, *ApJ*, 684, 226
 Teyssier R., 2002, *A&A*, 385, 337
 Trac H., Cen R., 2007, *ApJ*, 671, 1
 Trac H., Gnedin N. Y., 2009, 0906.4348
 Verner D. A., Ferland G. J., Korista K. T., Yakovlev D. G., 1996, *ApJ*, 465, 487
 Walch S., Whitworth A. P., Bisbas T. G., Wunsch R., Hubber D. A., 2013, *MNRAS*, 435, 917
 Whalen D., Norman M. L., 2008, *ApJ*, 673, 664
 Williams R. J. R., 1999, *MNRAS*, 310, 789
 Williams R. J. R., Henney W. J., 2009, *MNRAS*, 400, 263
 Wise J. H., Abel T., 2008, *ApJ*, 684, 1
 Wyithe S., Mould J., Loeb A., 2011, *ApJ*, 743, 173
 Yajima H., Choi J.-H., Nagamine K., 2012, *MNRAS*, 427, 2889
 Zaroubi S., 2013, *ASSL*, 396, 45

APPENDIX A: CONVERGENCE OF DIFFUSE RADIATION IN THE STROMGREN SPHERE PROBLEM

In this appendix, we discuss the convergence of our simulations of the expansion of an HII region including recombination radiation (Fig. 3). We present convergence tests at

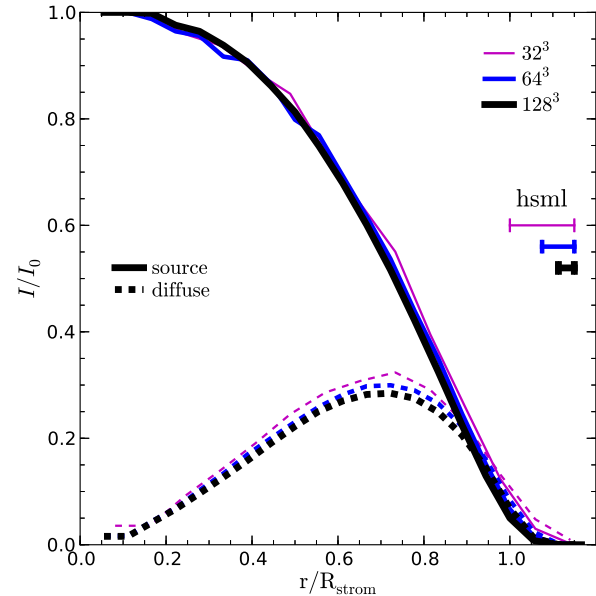


Figure A1. Convergence of the equilibrium intensity profile with spatial resolution. Symbols have the same meaning as in the bottom panels of Figure 2. A run using 128^3 SPH particles (black curves), i.e., the same number of particles as adopted in the runs discussed in Section 3 (and identical to the simulation including RT of recombination radiation discussed there), is compared to runs using 32^3 (magenta curves) and 64^3 (blue curves) particles. Lines to the right, marked “hsm1”, show the spatial resolution of each run, i.e. the average smoothing kernel of the particles. The runs using 128^3 and 64^3 particles are converged with respect to spatial resolution.

$t = 4t_{\text{rec}}$, i.e., in ionization equilibrium, which is the relevant case to compare our method to solutions discussed in the literature (Section 3). We note that the convergence at earlier times is equally good.

Figure A1 compares the run discussed in Section 3 and carried out using 128^3 (black curves; identical to the simulation including RT of recombination radiation shown in Figs. 2 and 3) with two lower-resolution runs employing 8 (magenta curves) and 64 (blue curves) times less particles to discretize the density field. The intensity profiles in the runs using 128^3 and 64^3 are nearly identical. The lowest resolution simulation using 32^3 particles yields an intensity that is significant out to slightly larger radii than in the higher resolution runs. However, the difference is within the size of the resolution element (see the smoothing length measures on the right hand side of the figure).

For the following convergence tests, a spatial resolution of 64^3 particles is adopted which, as we have just shown, yields converged results in terms of spatial resolution. In Figure A2, we compare a run using the time step used in Section 3 (black curve) with runs employing one order of magnitude shorter and longer time steps, $\Delta t = 0.01$ Myr and $\Delta t = 1$ Myr respectively. In all cases, the emission time step is $\Delta t_{\text{em}} = 0.1\Delta t$. All three runs give nearly identical results.

Finally, we investigate the impact of varying the angular resolution at which the RT is carried out. In Figure A3, we

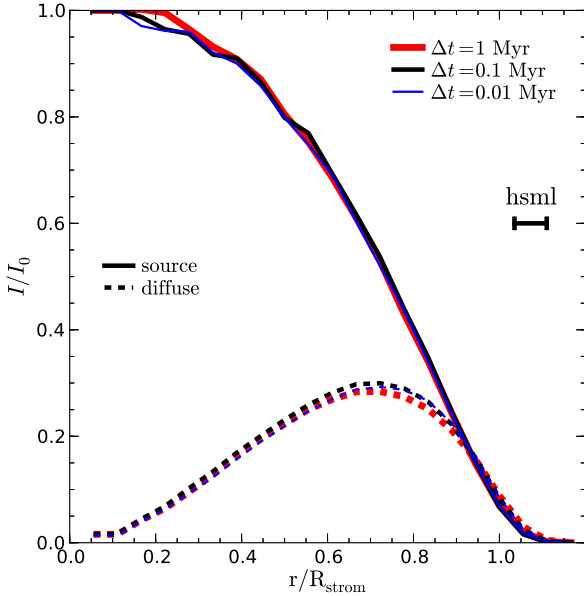


Figure A2. Convergence of the equilibrium intensity profile with the RT time step. Symbols have the same meaning as in the bottom panels of Figure 2. A run using $\Delta t = 0.1$ Myr (black curves), i.e., the time step adopted in the runs discussed in Section 3, is compared to runs with 10 times longer (red curves) and shorter (blue curves) time steps. In all runs, $\Delta t_{\text{em}} = 0.1\Delta t$. The run using $\Delta t = 0.1$ Myr is converged.

decrease the solid angle subtended by each transmission cone from $4\pi/8$ (black) to $4\pi/64$ (green) and $4\pi/128$ (yellow). Most of the small intensity differences seen in the runs at different angular resolutions are caused by the increasingly poorer angular sampling, which is because we kept $N_{\text{EC}} = N_{\text{RC}} = 8$ fixed while increasing the angular resolution (i.e., N_{TC}). Indeed, additional tests have shown that the small differences seen in Figure A3 disappear when the angular sampling is increased in step with the angular resolution, by increasing N_{EC} and N_{RC} , as expected given the spherical symmetry of the problem.

APPENDIX B: ADDING THE MISSING RECOMBINATION RADIATION INTENSITY TO THE SHADOWING TEST SETUP

In our simulations presented in Section 4, we assume that an infinitely extended plane-parallel front of ionizing radiation thought to originate from a source outside the box enters the box from one side and moves to ionize the simulation box, leaving a shadow behind the opaque obstacle present in the box. The source intensity driving the plane-parallel front determines the ionization balance inside the box, setting the mean free path of the ionizing photons and the distance out to which an I-front is driven. Because we require the entire box to be ionized, both the distance to the I-front and the mean free path must be larger than (or at least equal to) the length of the box. Here we show that this means that recombination radiation emitted from ionized gas outside the box contributes to the ionization balance inside the box (assum-

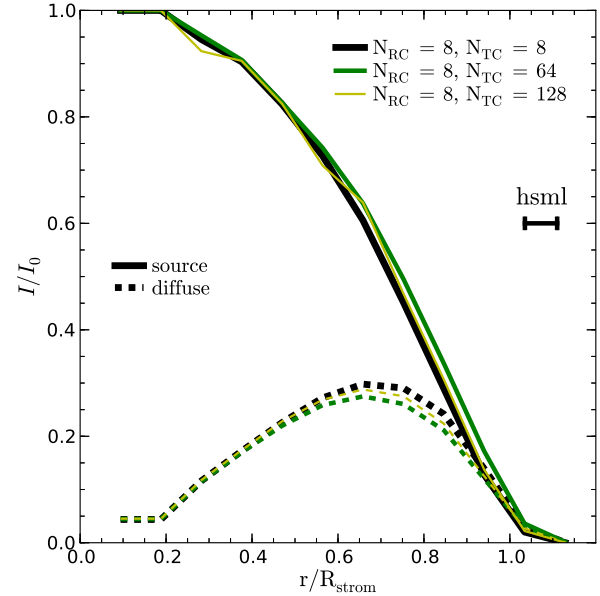


Figure A3. Convergence of the equilibrium intensity profile with angular resolution, expressed in terms of the number of transmission cones N_{TC} . Symbols have the same meaning as in the bottom panels of Figure 2. A run using $N_{\text{TC}} = 8$, i.e., the same angular resolution as employed in the runs discussed in Section 3, is compared with two runs using higher angular resolution, $N_{\text{TC}} = 64$ (green curves) and $N_{\text{TC}} = 128$ (yellow curves). All runs use $N_{\text{EC}} = N_{\text{RC}} = 8$ cones to emit stellar and recombination photons, respectively. The small differences between the runs result because we increased the angular resolution without increasing the angular sampling.

ing that the cross-sections for the absorption of stellar and recombination photons and hence the mean free paths are similar), and describe how we account for this contribution.

Consider a simulation box containing hydrogen-only gas with uniform number density n_{H} , illuminated by a plane-parallel radiation front of flux F , as in Section 4. Equilibrium between ionizations and recombinations implies

$$FA = \alpha_B n_{\text{H}}^2 A L_{\text{strom}}, \quad (\text{B1})$$

where A is the surface area of the box side through which the plane parallel radiation front of flux F is entering the box and L_{strom} , the Stromgren distance, is the distance that the I-front will penetrate (e.g., Gritschneider et al. 2009), given by

$$L_{\text{strom}} = \frac{F}{\alpha_B n_{\text{H}}^2}. \quad (\text{B2})$$

In our simulations, we require the Stromgren distance to be larger than the box side length L_{box} . We achieve this by setting the incoming flux F such that Eq. B2 gives $L_{\text{strom}} > L_{\text{box}}$. In ionization equilibrium, the choice of the flux F then implies a value for the ionized fraction of the gas determined using

$$\Gamma_{\text{ion}} n_{\text{H}} (1 - x_{\text{HII}}) = \alpha_B n_{\text{H}}^2 x_{\text{HII}}^2, \quad (\text{B3})$$

where $x_{\text{HII}} = 1 - x_{\text{HI}}$ is the ionized hydrogen fraction, x_{HI} the neutral hydrogen fraction, $\Gamma_{\text{ion}} = \sigma F$ the photoionization

rate of the incoming photons, and σ the photoionization cross-section. For simplicity, but without loss of generality, we consider the case of monochromatic radiation.

The recombination radiation emissivity per unit volume of gas with ionized fraction x_{HII} computed using Eq. B3 is

$$E_{\text{RR}} = \alpha_1 n_{\text{H}}^2 x_{\text{HII}}^2, \quad (\text{B4})$$

while the mean free path of recombination radiation through the same gas is

$$\lambda_{\text{mfp}} = (\sigma n_{\text{H}}(1 - x_{\text{HII}}))^{-1}. \quad (\text{B5})$$

The key issue is that, not surprisingly, L_{strom} and λ_{mfp} take very similar values. E.g., using the values for F and n_{H} assumed in Section 4 in Eqs. B2, B3 and B5 yields $L_{\text{strom}} = 1251.25 \text{ kpc}$ and $\lambda_{\text{mfp}} = 1251.37 \text{ kpc}$, i.e., $L_{\text{strom}} \approx \lambda_{\text{mfp}}$. This similarity causes a practical problem since in order for a point in the shadowed region to see the full intensity of the recombination radiation emitted by the surrounding gas, the computation box must be large enough to include a sphere of radius λ_{mfp} around the center of the shadow. Our setup assumes that the whole simulation box is ionized by the source flux, which implies $L_{\text{strom}} > L_{\text{box}}$. However, because $\lambda_{\text{mfp}} \approx L_{\text{strom}}$, it is not possible for the box of size L_{box} to contain a sphere with radius λ_{mfp} . Figure B1 illustrates the issue.

We account for the contribution to the intensity from recombining gas outside the box by inserting additional particles positioned at the four sides of the computational box parallel to the major axis of the shadow region, whom we then assign an appropriate luminosity. We do not place such boundary particles at the $x = 0$ side in order to have a strict control of the number of photons entering the box from the source side. We do not place boundary particles at the $x = L_{\text{box}}$ side because the shadow covers a portion of it. The luminosity of the boundary particles is set to reproduce the total number of recombination radiation photons through a surface with area A , emitted by the gas with uniform density n_{H} and ionized fraction given by Eq. B3. The associated intensity is given by the integral of all recombination radiation emitted by uniformly ionized gas of constant hydrogen density n_{H} arriving at the centre of a sphere with radius λ_{mfp} ,

$$I = 4\pi \int_0^{\lambda_{\text{mfp}}} \frac{E_{\text{RR}} e^{-\sigma n_{\text{H}} x_{\text{HI}} r}}{4\pi r^2} r^2 dr = 0.63 \lambda_{\text{mfp}} E_{\text{RR}}. \quad (\text{B6})$$

The fraction under the integral is the recombination radiation intensity coming from a single point at distance r and to obtain the final solution we used $\lambda_{\text{mfp}} = (\sigma n_{\text{H}} x_{\text{HI}})^{-1}$. The neutral fraction x_{HI} used here is the neutral fraction found in the gas in front of the barrier in a simulation that adopts the on-the-spot approximation. The boundary sources are distributed on a regular grid and switched on only after being overtaken by the I-front driven by the external source. The number of boundary sources is chosen to achieve numerical convergence. In the simulations in Section 4, we used 50^2 boundary sources per side. Note that for simplicity, we do not adjust the flux of recombination radiation emitted by the boundary particles at the 4 sides to compensate for the lack of emission from the 2 remaining sides. This approximation does not affect our conclusions, because we find that the shadow is highly ionized by recombination radiation even without such a compensation.

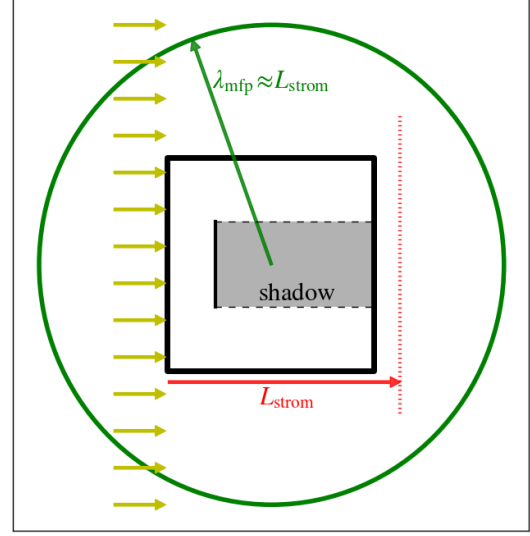


Figure B1. Diagram describing the issue of the shadowing test setup where some of the sources of recombination radiation are not encompassed by the simulation box. A plane-parallel radiation front assumed to extend infinitely in the directions perpendicular the direction of propagation (yellow arrows), enters the simulation box (thick solid black cube) from one side, causing the barrier in the box (thin solid black line) to cast a shadow behind it (gray shaded area bordered by dashed black lines). In order for the shadow to extend to the edge of the box, the Stromgren distance associated with the incoming plane parallel flux, L_{strom} (red dotted line), must be larger than the box, L_{box} . The plane-parallel flux intensity also determines the ionized fraction in the gas around the shadow, which in turn defines the mean free path of the ionizing recombination photons, λ_{mfp} (green solid arrow). Since we require that $L_{\text{strom}} \gtrsim L_{\text{box}}$, the region from which the recombination radiation can reach the shadow extends beyond the size of the simulation box (shown by the solid green circle), because $L_{\text{strom}} \approx \lambda_{\text{mfp}}$. In our simulations, the recombination radiation originating from outside the box is added by hand.